Accelerating gravitational-wave parametrized tests of general relativity using a multiband decomposition of likelihood

Naresh Adhikari[*] and Soichiro Morisaki[†]

Department of Physics, University of Wisconsin-Milwaukee, Milwaukee, Wisconsin 53201, USA

The detection of gravitational waves from compact binary coalescence (CBC) has allowed us to probe the strong-field dynamics of general relativity (GR). Among various tests performed by the LIGO-Virgo-KAGRA Collaboration are parametrized tests, where parametrized modifications to GR waveforms are introduced and constrained. This analysis typically requires the generation of more than millions of computationally expensive waveforms. The computational cost is higher for a longer signal, and current analyses take weeks to years to complete for a binary neutron star (BNS) signal. We present a technique to accelerate the parametrized tests using a multiband decomposition of likelihood, which was originally proposed by one of the authors to accelerate parameter estimation analyses of CBC signals assuming GR. We show that our technique speeds up the parametrized tests of a $1.4\,M_\odot$–$1.4\,M_\odot$ BNS signal by a factor of $\mathcal{O}(10)$ for a low-frequency cutoff of 20 Hz. We also verify the accuracy of our method using simulated signals and real data.

I. INTRODUCTION

The gravitational-wave era started with the discovery of the gravitational-wave signal from the binary black hole merger, GW150914 [1], by the advanced LIGO detectors [2–4]. The binary neutron star (BNS) signal, GW170817 [5], was observed two years later by the advanced LIGO and advanced Virgo [6,7] detectors. It became the first example of multimessenger observations involving gravitational waves [8,9]. Recently, the first-ever observations of mergers of two distinct compact objects, i.e., a neutron star and a black hole, were also achieved [10], completing the search for a gravitational-wave signal originating from all three distinct classes of compact mergers. The detected CBC signals enabled us to test general relativity (GR) in the strong-field regime. Various tests have been proposed and applied to the detected signals by the LIGO-Virgo-KAGRA Collaboration (LVK) [11–15] and others [16–18].

Among various tests performed by LVK are the parametrized tests [19–22]. In these tests, parametrized non-GR modifications are introduced to GR waveforms, and the parameters governing the modifications are constrained. The non-GR parameters consist of inspiral parameters and postinspiral parameters. The inspiral parameters parametrize relative or absolute shifts of the inspiral post-Newtonian coefficients, while the postinspiral parameters parametrize relative shifts of the postinspiral phenomenological parameters. For informative constraints to be obtained efficiently, typically only one of those non-GR parameters is allowed to deviate and be constrained in a single analysis [11,23]. Such a single-parameter test is known to be robust to ignorance of higher-order corrections [24]. Recent works [18,25] also showed that multiple parameters can be investigated simultaneously using principal component analysis. Those parametrized modifications can incorporate modifications predicted by various alternative theories of gravity, and we can map those constraints to filter such non-GR theories as a postprocessing step [26].

The parametrized tests typically employ stochastic sampling and require more than millions of likelihood evaluations. Each likelihood evaluation requires the evaluation of waveform values at all the frequency points considered, which is the dominant cost. Since the frequency points are sampled with an interval of $1/T$, where T is the duration of data, more waveform evaluations are required for a longer signal. For a $1.4\,M_\odot$–$1.4\,M_\odot$ BNS signal, current analyses take weeks to years without any approximate methods. This will be a serious problem when the sensitivities of detectors are improved and BNS signals are detected more frequently. The same problem arises for parameter estimation analyses of CBCs assuming GR, and various techniques have been proposed to reduce the computational cost of waveform generation [27–33].

Among the various rapid parameter estimation techniques, a recent work considered a multiband decomposition of the gravitational-wave likelihood [31], which exploits the chirping nature of the CBC signals and speeds up the parameter estimation of a BNS signal by more than

[*]naresh@uwm.edu
[†]morisaki@uwm.edu

104053-1

an order of magnitude. Since the signal frequency increases with time, the time to merger, $\tau(f)$, decreases with frequency f. This implies that the likelihood can be approximated into a form that can be computed with waveform values at frequency points sampled with a variable interval proportional to $1/\tau(f)$. This approximation drastically reduces the number of waveform evaluations at high frequency. A similar idea has been utilized for speeding up the matched-filter analysis for detection of CBC signals [34–36].

In this paper, we apply the multiband decomposition technique to parametrized tests of GR. In Sec. II, we briefly explain parametrized tests of GR and the multiband decomposition method for a GR signal. To extend the multiband decomposition method to parametrized tests, we need to consider modifications of $\tau(f)$ caused by non-GR modifications in waveforms. In Sec. III, we derive the modified $\tau(f)$ and investigate the speed-up gains of our technique for a BNS signal. In Sec. IV, we study the accuracy of our technique using simulated BNS signals and real data. Finally, we conclude our work in Sec. V.

II. BASICS

In this section, we explain the parametrized tests of GR and the multiband decomposition technique for rapid parameter estimation.

A. Parametrized tests of GR

The dominant quadrupole moment of gravitational waves is of the following form in the frequency domain,

$$\tilde{h}(f) = A(f)e^{i\Phi(f)}, \qquad (1)$$

where $A(f)$ and $\Phi(f)$ denote signal amplitude and phase, respectively. The phase evolution of the early inspiral part is calculated via the post-Newtonian (PN) expansion [37,38], which is an expansion with respect to a small orbital velocity v/c. A term with the order of $\mathcal{O}((v/c)^n)$ relative to the leading order is referred to as $(n/2)$PN. In GR, the phase up to the 3.5PN order is given by [39–41]

$$\Phi^{\mathrm{GR}}(f) = 2\pi f t_c - \phi_c - \frac{\pi}{4} + \sum_{j=0}^{7} [\varphi_j^{\mathrm{GR}} + \varphi_j^{\mathrm{GR}(l)} \ln f] f^{(j-5)/3},$$
$$(2)$$

where t_c and ϕ_c denote the coalescence time and phase, respectively, and φ_j^{GR} and $\varphi_j^{\mathrm{GR}(l)}$ are $(j/2)$PN coefficients depending on component masses m_1, m_2 and spins $\vec{S}_1$, $\vec{S}_2$. Note that φ_j^{GR} is vanishing for $j = 1$, and $\varphi_j^{\mathrm{GR}(l)}$ is vanishing except for $j = 5$, 6.

In the parametrized tests, parametrized deformations of nonzero PN coefficients are introduced by [19–22]

$$\varphi_j^{\mathrm{GR}} \to [1 + \delta\hat{\varphi}_j]\varphi_j^{\mathrm{GR}}, \qquad \varphi_j^{\mathrm{GR}(l)} \to [1 + \delta\hat{\varphi}_j^{(l)}]\varphi_j^{\mathrm{GR}(l)},$$

where $\delta\hat{\varphi}_j$ and $\delta\hat{\varphi}_j^{(l)}$ are non-GR parameters quantifying relative shifts of GR inspiral phasing. In addition to the relative shifts, absolute shifts are introduced to the -1PN,

$$\varphi_{-2}f^{-7/3} = \frac{3\delta\hat{\varphi}_{-2}}{128}\eta^{2/5}\left(\frac{\pi G\mathcal{M}f}{c^3}\right)^{-7/3}, \qquad (3)$$

and 0.5PN,

$$\varphi_1 f^{-4/3} = \frac{3\delta\hat{\varphi}_1}{128\eta^{1/5}}\left(\frac{\pi G\mathcal{M}f}{c^3}\right)^{-4/3}, \qquad (4)$$

where $\mathcal{M}$ and η are chirp mass and symmetric mass ratios, respectively,

$$\mathcal{M} = \frac{(m_1 m_2)^{3/5}}{(m_1 + m_2)^{1/5}}, \qquad \eta = \frac{m_1 m_2}{(m_1 + m_2)^2}. \qquad (5)$$

The -1PN term is used to model gravitational dipole radiation predicted by alternative theories of gravity [42]. The full list of inspiral non-GR parameters is

$$\left\{\delta\hat{\varphi}_{-2}, \delta\hat{\varphi}_0, \delta\hat{\varphi}_1, \delta\hat{\varphi}_2, \delta\hat{\varphi}_3, \delta\hat{\varphi}_4, \delta\hat{\varphi}_5^{(l)}, \delta\hat{\varphi}_6, \delta\hat{\varphi}_6^{(l)}, \delta\hat{\varphi}_7\right\}.$$

The 2.5PN parameter $\delta\hat{\varphi}_5$ is not included since it is completely degenerate with ϕ_c.

In addition to the deformations of the inspiral phase, parametrized deformations of the postinspiral phase are also considered. The IMRPhenom waveform model [43–45] employs phase ansatz parametrized by β_i ($i = 0$, 1, 2, 3) for the intermediate stage and by α_i ($i = 0, 1, 2, 3$, 4) for the merger-ringdown stage. Relative shifts to those parameters are introduced in a similar way, which are parametrized by $\delta\hat{\beta}_i$ and $\delta\hat{\alpha}_i$. The full list of postinspiral non-GR parameters as considered in [11,13–15] is

$$\{\delta\hat{\alpha}_2, \delta\hat{\alpha}_3, \delta\hat{\alpha}_4, \delta\hat{\beta}_2, \delta\hat{\beta}_3\}.$$

For meaningful constraints to be obtained efficiently, typically only one of those 15 non-GR parameters is allowed to deviate and be constrained in a single analysis. Parametrized deformations of amplitude can also be considered, but they are difficult to be measured with the current generation of detectors [46–48].

The non-GR parameters are estimated or constrained via Bayesian inference. In the Bayesian inference, the posterior distribution $p(\boldsymbol{\theta}|\{\boldsymbol{d}_i\})$ is calculated via the Bayes theorem:

$$p(\boldsymbol{\theta}|\{\boldsymbol{d}_i\}) \propto \mathcal{L}(\{\boldsymbol{d}_i\}|\boldsymbol{\theta})\pi(\boldsymbol{\theta}), \qquad (6)$$

where $\boldsymbol{d}_i$ denotes the data taken from the ith detector, $\boldsymbol{\theta}$ the set of model parameters consisting of one of the non-GR

parameters and GR parameters, $\pi(\boldsymbol{\theta})$ the prior distribution function determined from our belief or prior knowledge on $\boldsymbol{\theta}$, and $\mathcal{L}(\boldsymbol{d}|\boldsymbol{\theta})$ the likelihood function. For the likelihood, the Gaussian-noise likelihood function is typically used [49,50],

$$\mathcal{L}(\{\boldsymbol{d}_i\}|\boldsymbol{\theta}) \propto \exp\left[-\frac{1}{2}\sum_i \|\boldsymbol{d}_i - \boldsymbol{h}_i(\boldsymbol{\theta})\|_i^2\right], \qquad (7)$$

where $\boldsymbol{h}_i$ is a model signal observed at the ith detector. Note that $\|\cdot\|^2 = (\cdot, \cdot)$ is the norm induced by the inner product,

$$(\boldsymbol{a}, \boldsymbol{b})_i = \frac{4}{T}\Re\left[\sum_{k=f_{\text{low}}T}^{f_{\text{high}}T} \frac{\tilde{a}^*(f_k)\tilde{b}(f_k)}{S_i(f_k)}\right], \qquad (8)$$

where f_{low} and f_{high} are the low- and high-frequency cutoffs of the analysis, respectively, T is the duration of data, $S_i(f)$ is the noise power spectral density of the ith detector, and $f_k \equiv k/T$ is the kth frequency bin. The logarithm of likelihood can be written as

$$\ln\mathcal{L}(\boldsymbol{d}|\boldsymbol{\theta}) = \sum_i\left[(\boldsymbol{d}_i, \boldsymbol{h}_i(\boldsymbol{\theta}))_i - \frac{1}{2}(\boldsymbol{h}_i(\boldsymbol{\theta}), \boldsymbol{h}_i(\boldsymbol{\theta}))_i\right] + \text{const}, \qquad (9)$$

where the constant part does not depend on $\boldsymbol{\theta}$ and is irrelevant for stochastic sampling.

The inference is typically done via stochastic sampling methods, such as Markov-chain Monte Carlo (MCMC) [51,52] and nested sampling [53]. The nonconstant term is computed millions of times during stochastic sampling. As evident from Eqs. (9) and (8), each likelihood evaluation requires evaluations of waveform values at all the frequency points from f_{low} to f_{high}. Those waveform evaluations are typically the dominant cost of analysis. The cost is proportional to the number of frequency points,

$$K_{\text{orig}} = (f_{\text{high}} - f_{\text{low}})T + 1, \qquad (10)$$

and higher for a longer signal.

B. Multiband decomposition

In the multiband decomposition method, the total frequency range is divided into B overlapping frequency bands $f_s^{(b)} \le f \le f_e^{(b)}(b = 0, 1, \ldots, B-1)$. The start and end frequencies are determined based on a user-specified sequence of durations, $T = T^{(0)} > T^{(1)} > \ldots > T^{(B-1)}$. First, the following equation is solved with respect to $f^{(b)}$ for each $b \in \{1, 2, \ldots, B-1\}$,

$$\tau(f^{(b)}) + L\sqrt{-\tau'(f^{(b)})} = T^{(b)} + t_{c,\text{min}} - T, \qquad (11)$$

where $\tau(f)$ is a reference time to merger from a gravitational-wave frequency f, and L is a user-specified constant controlling the accuracy of the approximation. A larger value of L gives more accurate likelihood values. Here, $t_{c,\text{min}}$ is the minimum coalescence time in the prior range, and $L = 5$ and $T - t_{c,\text{min}} = 2.12$ s are used throughout this paper, following [31]. The start and end frequencies are determined as

$$f_s^{(b)} = \begin{cases} f_{\text{low}} & (b = 0) \\ f^{(b)} - \frac{1}{\sqrt{\tau'(f^{(b)})}} & (b > 0) \end{cases} \qquad (12)$$

$$f_e^{(b)} = \begin{cases} f^{(b+1)} & (b < B - 1) \\ f_{\text{high}} + \Delta f_{\text{high}} & (b = B - 1). \end{cases} \qquad (13)$$

This way of constructing frequency bands guarantees that the inverse Fourier transform of $\tilde{h}(f)$ starting from $f_s^{(b)}$ has a duration shorter than $T^{(b)}$. Here, $\Delta f_{\text{high}} > 0$ is required to avoid the loss of accuracy caused by the abrupt termination of a waveform.

With the frequency bands constructed, $(\boldsymbol{d}_i, \boldsymbol{h}_i)_i$ is approximated into the following form,

$$(\boldsymbol{d}_i, \boldsymbol{h}_i(\boldsymbol{\theta}))_i$$
$$\simeq \sum_{b=0}^{B-1} \frac{4}{T^{(b)}}\Re\left[\sum_{k=\lceil f_s^{(b)}T^{(b)}\rceil}^{\lfloor f_e^{(b)}T^{(b)}\rfloor} w^{(b)}(f_k^{(b)})\tilde{D}_{i,k}^{(b)*}\tilde{h}_i(f_k^{(b)};\boldsymbol{\theta})\right], \qquad (14)$$

where $w^{(b)}(f)$ is a smooth window function extracting waveform values in the bth frequency band, $\tilde{D}_{i,k}^{(b)}$ is a quantity calculated from data and power spectral density, and

$$f_k^{(b)} \equiv \frac{k}{T^{(b)}}. \qquad (15)$$

The sum over a high-frequency band requires waveform values only at downsampled frequencies whose interval is $1/T^{(b)}$, and hence fewer waveform evaluations. The number of waveform evaluations required for a single evaluation of $(\boldsymbol{d}_i, \boldsymbol{h}_i(\boldsymbol{\theta}))_i$ is reduced to

$$K_{\text{MB}} = \sum_{b=0}^{B-1}(\lfloor f_e^{(b)}T^{(b)}\rfloor - \lceil f_s^{(b)}T^{(b)}\rceil + 1). \qquad (16)$$

There were two approximate methods proposed to compute $(\boldsymbol{h}_i(\boldsymbol{\theta}), \boldsymbol{h}_i(\boldsymbol{\theta}))_i$ with fewer waveform evaluations. One method is referred to as linear interpolation, which approximates $|\tilde{h}_i(f;\boldsymbol{\theta})|^2$ as a linear interpolation of the squares of downsampled waveform values. This works well

if the waveform model contains only dominant quadrupole moments, where $|\tilde{h}_i(f;\boldsymbol{\theta})|^2$ is a smooth function. The other method is referred to as IFFT-FFT, which works even if the waveform model contains multiple moments. In either case, $(\boldsymbol{h}_i(\boldsymbol{\theta}), \boldsymbol{h}_i(\boldsymbol{\theta}))_i$ is computed with waveform values at the K_{MB} frequency points, and no additional waveform evaluations are required. Thus, the cost of a single likelihood evaluation is reduced by $K_{\mathrm{orig}}/K_{\mathrm{MB}}$.

III. EXTENSION TO PARAMETRIZED TESTS

In the previous work [31], which applies the multiband decomposition method to the analysis of a GR signal, the 0PN formula of $\tau(f)$ in GR is used for solving (11). For extending the previous work to parametrized tests of GR, we need to take into account corrections of $\tau(f)$ from the parametrized modifications of inspiral phasing. In this section, we derive the modified formula of $\tau(f)$ taking them into account. We also apply it for setting up frequency bands and study the speed-up gains of our method for a typical BNS signal.

A. Modified time to merger

In order to get the modified time-to-merger formula, we use the following condition in accordance with the stationary phase approximation [40,54–56]:

$$\Phi(f) = -\Psi(t(f)) + 2\pi f t(f) + \frac{\pi}{4}, \qquad (17)$$

where $\Psi(t)$ is the phase of a time-domain waveform and $t(f)$ is the time at which $\Psi'(t) = 2\pi f$. Hence, we can now relate $t(f)$ to the derivative of $\Phi(f)$,

$$t(f) = \frac{\Phi'(f)}{2\pi}. \qquad (18)$$

With the phase formula at the inspiral part, we obtain the following modified time-to-merger formula,

$$
\begin{aligned}
\tau(f) &= t_c - t(f) \\
&= \frac{1}{2\pi}\left\{ \frac{7\varphi_{-2}}{3f^{10/3}} + \frac{5(1+\delta\hat{\varphi}_0)\varphi_0^{\mathrm{GR}}}{3f^{8/3}} + \frac{4\varphi_1}{3f^{7/3}} + \frac{(1+\delta\hat{\varphi}_2)\varphi_2^{\mathrm{GR}}}{f^2} + \frac{2(1+\delta\hat{\varphi}_3)\varphi_3^{\mathrm{GR}}}{3f^{5/3}} + \frac{(1+\delta\hat{\varphi}_4)\varphi_4^{\mathrm{GR}}}{3f^{4/3}} \right. \\
&\quad \left. - \frac{(1+\delta\hat{\varphi}_5^{(l)})\varphi_5^{(l)\mathrm{GR}}}{f} - \frac{(1+\delta\hat{\varphi}_6)\varphi_6^{\mathrm{GR}} + (1+\delta\hat{\varphi}_6^{(l)})\varphi_6^{(l)\mathrm{GR}}(\ln f + 3)}{3f^{2/3}} - \frac{2(1+\delta\hat{\varphi}_7)\varphi_7^{\mathrm{GR}}}{3f^{1/3}} \right\}.
\end{aligned} \qquad (19)
$$

Since the time to merger is predominantly determined by the terms up to 0PN, we ignore terms higher than that order and employ the following formula,

$$\tau(f) = \frac{7\varphi_{-2}}{6\pi f^{10/3}} + \frac{5(1+\delta\hat{\varphi}_0)\varphi_0^{\mathrm{GR}}}{6\pi f^{8/3}} \qquad (20)$$

$$
\begin{aligned}
&= \frac{7\delta\hat{\varphi}_{-2}}{256\pi}\eta^{2/5}\left(\frac{\pi G\mathcal{M}}{c^3}\right)^{-7/3} f^{-10/3} \\
&\quad + \frac{5(1+\delta\hat{\varphi}_0)}{256\pi}\left(\frac{\pi G\mathcal{M}}{c^3}\right)^{-5/3} f^{-8/3}.
\end{aligned} \qquad (21)
$$

If higher-order multiple moments are present, the same formula with the frequency rescaling, $f \to 2f/m$, is used, where m is the maximum magnetic number of the moments.

For validating our approximate time-to-merger formula, we numerically calculate time-domain waveforms incorporating higher-order PN terms and compare their durations with predictions from our formula. Figure 1 shows time-domain waveforms for nonspinning $1.4\,M_\odot$–$1.4\,M_\odot$ BNS with various values of $\delta\hat{\varphi}_0$ or $\delta\hat{\varphi}_{-2}$. They are calculated as the inverse Fourier transforms of frequency-domain waveforms from 20 Hz to 1024 Hz that include

terms up to the 3.5PN order in phase and the leading-order term in amplitude. The GR phase coefficients have been calculated with SimInspiralTaylorF2AlignedPhasing implemented in the LIGO Algorithmic Library (LAL) [57]. The vertical lines represent predictions from our approximate time-to-merger formula with $f = 20$ Hz. As seen in the figure, vertical lines accurately locate the time when waveforms start, demonstrating that our approximate time-to-merger formula is accurate enough.

Evaluating Eq. (21) demands a choice on the values of $\mathcal{M}, \eta, \delta\hat{\varphi}_0$, and $\delta\hat{\varphi}_{-2}$. To guarantee that the duration of each frequency band is long enough for any template waveform generated during stochastic sampling, their values are chosen to maximize $\tau(f)$. Hence, the minimum value of $\mathcal{M}$ and the maximum values of $\eta, \delta\hat{\varphi}_0$, and $\delta\hat{\varphi}_{-2}$ within the explored parameter space are chosen. The maximum value of η is typically 1/4, which corresponds to $m_1 = m_2$.

From Eq. (21), it is clear that $\tau(f)$ becomes negative for $\delta\hat{\varphi}_0 < -1$ or $\delta\varphi_{-2} < 0$ unless the other terms are significant enough to compensate it. In this case, the template waveform is an inverse-chirp waveform, which starts from $t = t_c$ and whose frequency simply decreases. The multiband approximation clearly breaks down for this type of waveform since it assumes that the signal frequency simply increases. Even without the multiband approximation, the
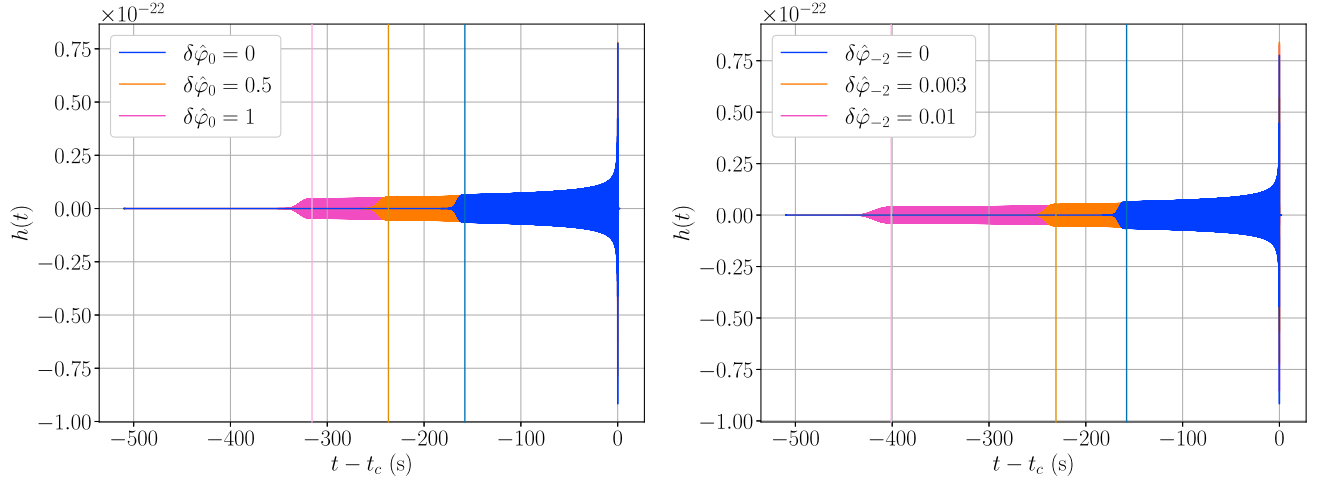
FIG. 1. Time-domain gravitational waveforms of nonspinning $1.4\,M_\odot$–$1.4\,M_\odot$ BNS starting from 20 Hz with various values of $\delta\hat{\varphi}_0$ (left) or $\delta\hat{\varphi}_{-2}$ (right). Vertical lines represent durations calculated by the up-to-0PN time-to-merger formula (21).

inverse-chirp signal is not properly analyzed in the analysis with the standard data conditioning [58], where only data up to ~ 2 seconds after t_c are analyzed.

Since the higher-order terms are ignored in Eq. (21), the huge deviations from GR in one or more of the higher-order terms can make the approximate time-to-merger formula inaccurate. In a typical analysis, the explored range of $\mathcal{M}$ is much wider than the width of its marginal posterior distribution, and the time to merger computed with the minimum $\mathcal{M}$ in the explored range is large enough to construct conservative frequency bands. The same argument can be made for hidden modifications with non-PN frequency dependence considered in [20]. Also, it is straightforward to take into account higher-order terms from Eq. (19) when huge deviations of higher-order terms are considered.

B. Speed-up gains

Table I shows speed-up gains of our multiband technique for a $1.4\,M_\odot$–$1.4\,M_\odot$ BNS signal with several choices of T

TABLE I. Numbers of original frequency points K_{orig}, the numbers of multibanded frequency points K_{MB}, and speed-up gains $K_{\mathrm{orig}}/K_{\mathrm{MB}}$ for a $1.4\,M_\odot$–$1.4\,M_\odot$ BNS signal with several choices of data duration T and a non-GR parameter value $\delta\hat{\varphi}_i$ used for calculating time to merger. The total frequency range is 20–2048 Hz, divided into frequency bands with $\{T^{(b)}\}_{b=0}^{B-1} = \{T, T/2, T/4, \ldots, 4\ \mathrm{s}\}$.

	$\delta\hat{\varphi}_i$	$T(\mathrm{s})$	K_{orig}	K_{MB}	Speed-up
GR	0	256	5.2×10^5	1.2×10^4	4.5×10^1
0PN ($i = 0$)	20	256	5.2×10^5	2.8×10^4	1.8×10^1
	20	4096	8.3×10^6	6.8×10^4	1.2×10^2
$-$1PN ($i = -2$)	1	256	5.2×10^5	3.6×10^4	1.4×10^1
	1	32768	6.6×10^7	3.2×10^5	2.1×10^2

and $\delta\hat{\varphi}_i$ used for calculating $\tau(f)$. For each case in the table, frequency bands were set up with the algorithm described in Sec. II B and Eq. (21) calculated with $m_1 = m_2 = 1.4\,M_\odot$ and $\delta\hat{\varphi}_i$ of the row. The total frequency range is 20–2048 Hz, and the durations of bands are powers of two, $\{T^{(b)}\}_{b=0}^{B-1} = \{T, T/2, T/4, \ldots, 4\ \mathrm{s}\}$. The speed-up gain is estimated by the reduction of frequency points, $K_{\mathrm{orig}}/K_{\mathrm{MB}}$. For setting up frequency bands, we utilized the existing implementation of the multiband decomposition method, MBGravitationalWaveTransient, available in the bilby [59,60] software.

For this study, we consider the three choices of $\delta\hat{\varphi}_i$: GR ($\delta\hat{\varphi}_0 = \delta\hat{\varphi}_{-2} = 0$) for reference, 0PN ($\delta\hat{\varphi}_0 = 20, \delta\hat{\varphi}_{-2} = 0$), and $-$1PN ($\delta\hat{\varphi}_0 = 0, \delta\hat{\varphi}_{-2} = 1$). Here, $\delta\hat{\varphi}_0 = 20$ or $\delta\hat{\varphi}_{-2} = 1$ is the maximum of its range explored by LVK analyses, which we have found in configuration files available at [61]. In a standard LVK parametrized test, the duration of analyzed data is the same as that used for GR parameter estimation regardless of the explored range of a non-GR parameter. For a $1.4\,M_\odot$–$1.4\,M_\odot$ BNS signal, $T = 256$ s. In either case with $T = 256$ s in the table, the speed-up gain is $\mathcal{O}(10)$. The speed-up gain for 0PN or $-$1PN is smaller than that for GR because $\tau(f)$ gets larger due to the non-GR modification.

To properly analyze any waveform within the explored range of a non-GR parameter, the data duration should be longer than the longest duration of the waveform with the allowed non-GR modifications. If data durations are determined in this conservative way, $T = 4096$ s and $T = 32768$ s for 0PN and $-$1PN respectively. With the conservative choice of T, the speed-up gain gets larger and is $\mathcal{O}(10^2)$ for either case.

IV. VALIDATION

In this section, we study the accuracy of our technique using simulated BNS signals and real data.

TABLE II. Injection values, prior, and explored range of GR parameters: Chirp mass $\mathcal{M}$, mass ratio $q \leq 1$, luminosity distance D_L, right ascension (RA) and declination (DEC), orbital inclination angle θ_{JN}, polarization angle ψ, constant phase ϕ_c, and coalescence time t_c. Here, $t_{c,\text{inj}}$ denotes the injection value of t_c, and it is set to the GPS time of 1187008882 (17 Aug 2017, 12:41:04 UTC).

Parameter	Unit	Injection value	Prior	Minimum	Maximum
$\mathcal{M}$	$M_\odot$	1.2	Uniform	1.15	1.25
q	$\cdots$	0.8	Uniform	0.125	1
θ_{JN}	Radian	0.4	Sine	0	π
D_L	Mpc	72	Comoving	10	100
RA	Radian	3.45	Uniform	0	2π
DEC	Radian	-0.40	Cosine	$-\pi/2$	$\pi/2$
ψ	Radian	0.65	Uniform	0	π
ϕ_c	Radian	1.3	Uniform	0	2π
$t_c - t_{c,\text{inj}}$	s	0	Uniform	-0.1	$+0.1$

A. Simulation study

To verify that the multiband approximation does not bias the inference, we simulate BNS signals with nonzero $\delta\hat{\varphi}_i$ and perform parametrized tests on them with and without the multiband decomposition method. The injection values, prior, and explored range of GR parameters are common among simulations, and they are outlined in Table II. The effects of spin angular momenta and tidal deformation of colliding objects are not taken into account for quick runs. We consider the network of the two advanced LIGO detectors and the Virgo detector, and inject signals into Gaussian noise colored by their design sensitivities. The analyzed frequency range is 20–2048 Hz. The network signal-to-noise ratios (SNRs) of the simulated signals are ~50. The simulated signals are computed with the TaylorF2 [39,62] waveform model implemented in LAL, and the same waveform model is used for parameter recovery.

In this study, we consider two simulated signals: the 0PN simulation with $\delta\hat{\varphi}_0 = 1$, $\delta\hat{\varphi}_i = 0(i \neq 0)$, and the -1PN simulation with $\delta\hat{\varphi}_{-2} = 0.003$, $\delta\hat{\varphi}_i = 0(i \neq -2)$. The duration of a signal from 20 Hz with vanishing non-GR parameters is ~160 s. It is doubled for the 0PN simulation or increased by ~50% for the -1PN simulation due to the nonzero GR parameter. The explored parameter range is $-1 \leq \delta\hat{\varphi}_0 \leq 2$ for the 0PN simulation and $-0.01 \leq \delta\hat{\varphi}_{-2} \leq 0.01$ for the -1PN simulation. For each simulation, the

FIG. 2. One- and two-dimensional marginal posterior distributions of chirp mass $\mathcal{M}$, mass ratio q, and 0PN relative deviation $\delta\hat{\varphi}_0$ from runs without (blue) and with (orange) the multiband decomposition technique. Diagonal panels show one-dimensional marginal posterior distributions, and vertical dashed lines indicate the 90% credible intervals. Off-diagonal panels show two-dimensional marginal posterior distributions, and solid lines indicate the 50% and 90% credible regions. Red lines indicate the injection values.
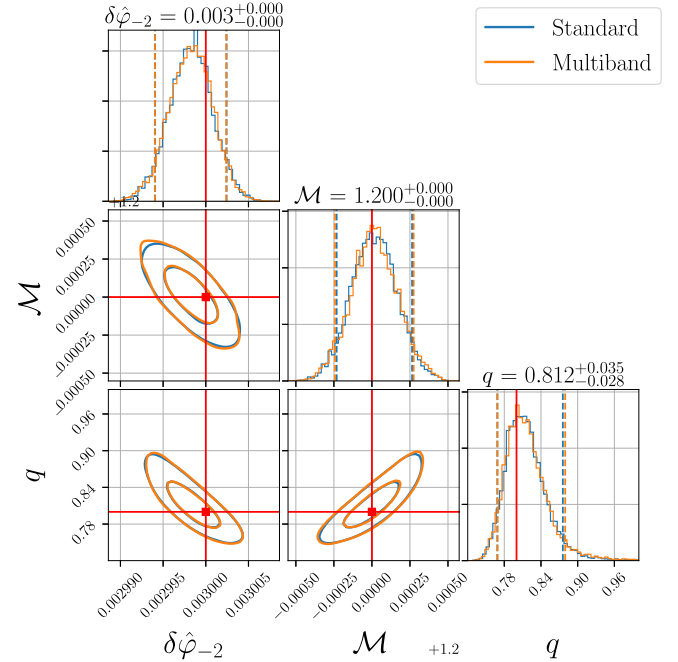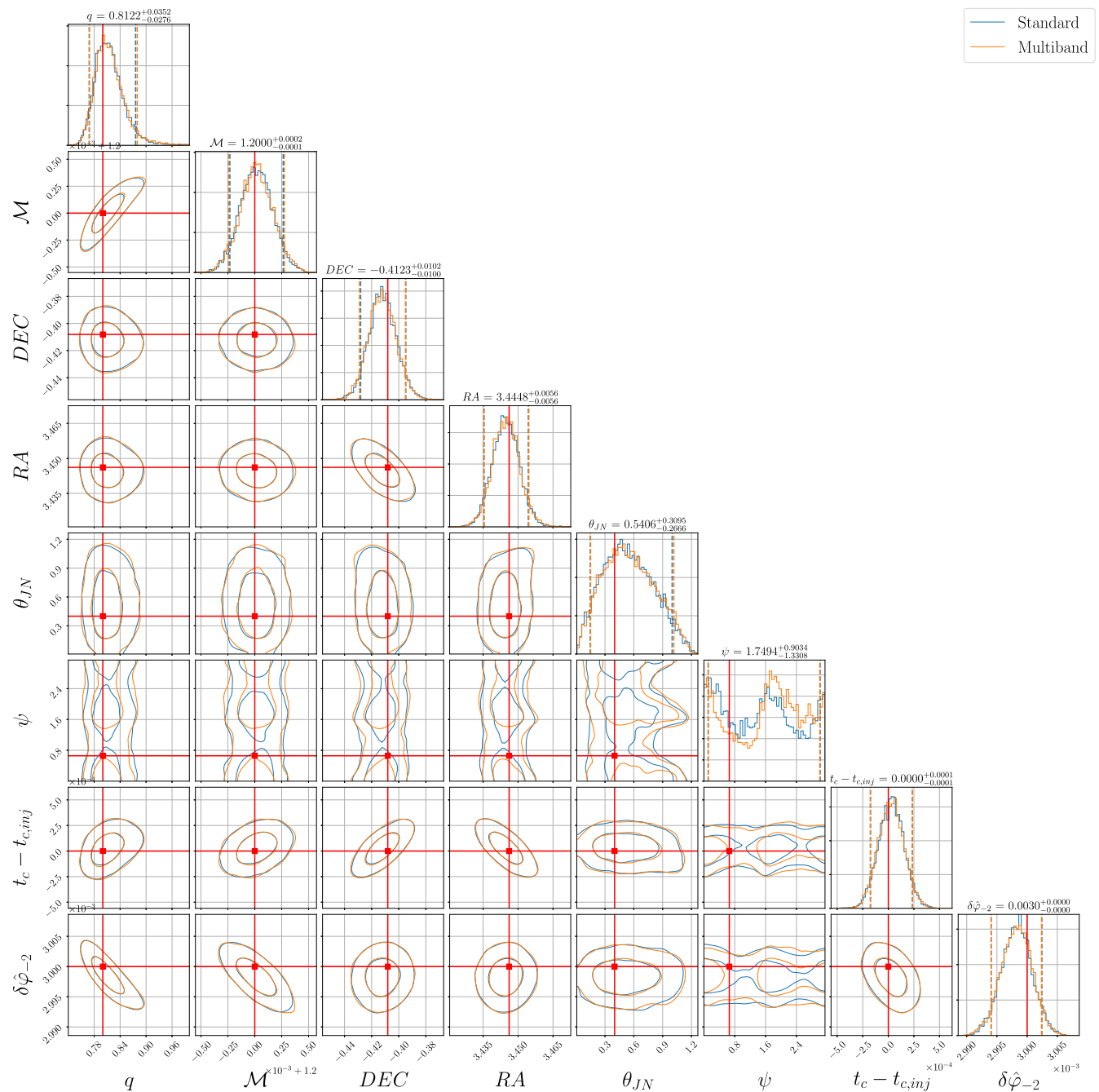
FIG. 3. One- and two-dimensional marginal posterior distributions of chirp mass $\mathcal{M}$, mass ratio q, and -1PN absolute deviation $\delta\hat{\varphi}_{-2}$ from runs without (blue) and with (orange) the multiband decomposition technique. Diagonal panels show one-dimensional marginal posterior distributions, and vertical dashed lines indicate the 90% credible intervals. Off-diagonal panels show two-dimensional marginal posterior distributions, and solid lines indicate the 50% and 90% credible regions. Red lines indicate the injection values.
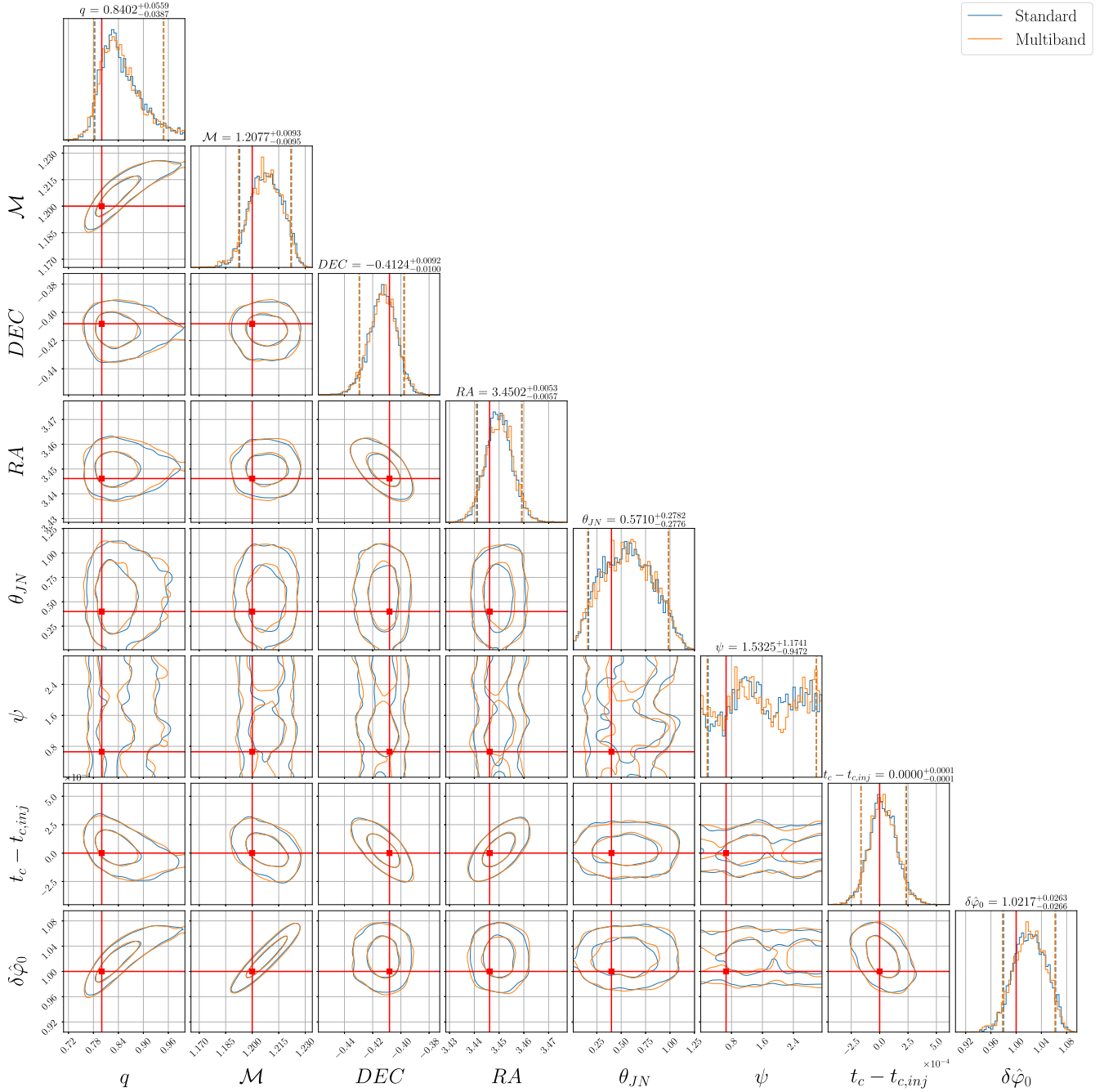
FIG. 4. One- and two-dimensional marginal posterior distributions of all the inferred parameters for the $-1\mathrm{PN}$ simulation from runs without (blue) and with (orange) the multiband decomposition technique. Diagonal panels show one-dimensional marginal posterior distributions, and vertical dashed lines indicate the 90% credible intervals. Off-diagonal panels show two-dimensional marginal posterior distributions, and solid lines indicate the 50% and 90% credible regions. Red lines indicate the injection values.

prior of the non-GR parameter is uniform over its explored range.

The durations of analyzed data are 512 s and 256 s for the 0PN and $-1\mathrm{PN}$ simulations, respectively. The total frequency range is divided into eight frequency bands with $\{T^{(b)}\}_{b=0}^{7} = \{512\text{ s}, 256\text{ s}, \ldots, 4\text{ s}\}$ for the multiband run of the 0PN simulation, and seven frequency bands with

$\{T^{(b)}\}_{b=0}^{6} = \{256\text{ s}, 128\text{ s}, \ldots, 4\text{ s}\}$ for the $-1\mathrm{PN}$ simulation. The speed-up gains $K_{\mathrm{orig}}/K_{\mathrm{MB}}$ are 58 and 37 for the 0PN and $-1\mathrm{PN}$ simulations, respectively.

The stochastic sampling is performed with the bilby software and the dynesty [63] sampler. The convergence of sampling is controlled by the number of live points n_{live} and the length of the MCMC chain in units

FIG. 5. One- and two-dimensional marginal posterior distributions of all the inferred parameters for the 0PN simulation from runs without (blue) and with (orange) the multiband decomposition technique. Diagonal panels show one-dimensional marginal posterior distributions, and vertical dashed lines indicate the 90% credible intervals. Off-diagonal panels show two-dimensional marginal posterior distributions, and solid lines indicate the 50% and 90% credible regions. Red lines indicate the injection values.

of its autocorrelation length n_{ACT} [60]. We use $n_{\mathrm{live}} = 500, n_{\mathrm{ACT}} = 10$ and $n_{\mathrm{live}} = 1000, n_{\mathrm{ACT}} = 10$ for the 0PN and -1PN simulations, respectively. We have confirmed that increasing their values does not change the results significantly, which means the results are converged. We marginalized the posterior over constant phase ϕ_c analytically and the luminosity distance D_{L} using the look-up table method [49,64].

Figures 2 and 3 show marginal posterior distributions of chirp mass ($\mathcal{M}$), mass ratio (q), and a non-GR parameter ($\delta\hat{\varphi}_0$ or $\delta\hat{\varphi}_{-2}$) for the 0PN and -1PN simulations, respectively. The runs without and with the multiband approximation are labeled "Standard" and "Multiband," respectively. As shown in the figures, the standard and multiband runs produce almost equivalent results in either simulation. More quantitatively, the differences in the lower
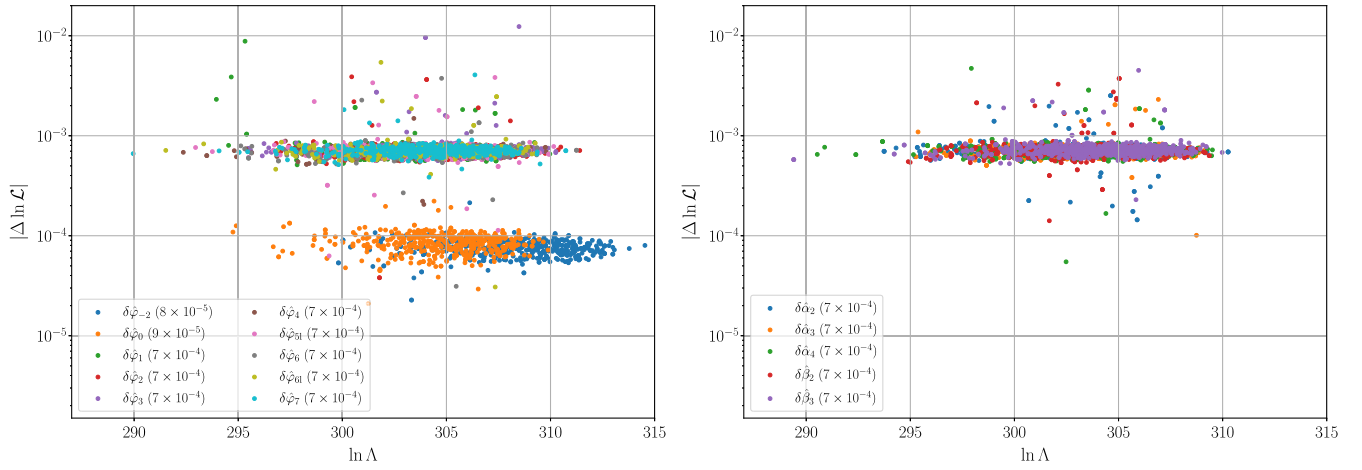
FIG. 6.   Log-likelihood errors $|\Delta \ln \mathcal{L}|$ of the multiband approximation calculated on posterior samples from GW190814. The left plot shows the errors for tests of inspiral non-GR parameters, and the right shows those for tests of postinspiral non-GR parameters. Each label shows the median value of these errors.

or upper bounds of the 90% credible intervals are less than 4% of their widths. Those observations indicate that the multiband approximation is accurate enough for a relatively high SNR of ∼50. Since log-likelihood errors introduced by the multiband approximation are roughly proportional to the square of SNR, they are smaller for lower SNR values. Therefore, our results show that our multiband approximation can also be safely used for SNR values below 50. The full posterior distributions of all the inferred parameters are presented in Figs. 4 and 5.

The standard runs take ∼9 days and ∼14 days to complete for the 0PN and −1PN simulations, respectively. They are reduced to ∼2 hours and ∼7 hours, respectively, with the multiband approximation. The reduction of run times is more or less consistent with the speed-up gains estimated from $K_{\mathrm{orig}}/K_{\mathrm{MB}}$. The runs are performed with an Intel Xeon Gold 6136 CPU with a clock rate of 3.0 GHz. The stochastic sampling is parallelized with 48 processes for the 0PN simulation, and 24 processes for the −1PN simulation.

B. Likelihood errors for GW190814

For validating our approximation with more complicated signal morphology, we investigate the likelihood errors of our approximation for GW190814 [65]. We compute $\ln \mathcal{L}$ with and without our approximation on posterior samples from LIGO-Virgo parameter estimation analysis, and we compute their differences $\Delta \ln \mathcal{L}$ as errors. This signal is an appropriate test case for validating our approximation with gravitational-wave higher-order multiple moments since their effects are statistically significant for this signal [65]. We also consider the calibration uncertainties of detectors for validating our approximation with signal modulation caused by them. The data are obtained from the Gravitational Wave Open Science Center [66], and posterior samples are

from [61]. The IMRPhenomPv3HM [67,68] waveform model is employed for likelihood evaluations, which is the same model used for the LVK analysis.

Figure 6 shows $|\Delta \ln \mathcal{L}|$, with the horizontal axis representing the nonconstant part of $\ln \mathcal{L}$,

$$\ln \Lambda \equiv \sum_i \left[(\boldsymbol{d}_i, \boldsymbol{h}_i)_i - \frac{1}{2}(\boldsymbol{h}_i, \boldsymbol{h}_i)_i \right]. \qquad (22)$$

The left plot shows the errors for tests of inspiral parameters, and the right shows those for tests of postmerger parameters. The total frequency range of 20–1024 Hz is divided into three frequency bands with $\{T^{(b)}\}_{b=0}^2 = \{16\,\mathrm{s}, 8\,\mathrm{s}, 4\,\mathrm{s}\}$. The frequency bands are determined based on the time to merger of the $m = 4$ mode, and with the following reference values of $\mathcal{M}$, η, $\delta\hat{\varphi}_0$, and $\delta\hat{\varphi}_{-2}$,

$$\mathcal{M} = 5.5\,M_\odot, \qquad \eta = 0.25,$$

$$\delta\hat{\varphi}_0 = \begin{cases} 20 & (\text{test of } \delta\hat{\varphi}_0) \\ 0 & (\text{otherwise}), \end{cases}$$

$$\delta\hat{\varphi}_{-2} = \begin{cases} 1 & (\text{test of } \delta\hat{\varphi}_{-2}) \\ 0 & (\text{otherwise}). \end{cases} \qquad (23)$$

Those reference values are determined based on the parameter range explored by the LVK analysis. The speed-up gain is 2.42 for the test of $\delta\hat{\varphi}_0$, 2.44 for the test of $\delta\hat{\varphi}_{-2}$, and 3.28 for the other cases. The IFFT-FFT algorithm is employed for computing $(\boldsymbol{h}, \boldsymbol{h})_i$ due to significant higher-order multiple moments.

Each plot label shows the median value of $|\Delta \ln \mathcal{L}|$. The errors are $\lesssim 10^{-4}$ for the test of $\delta\hat{\varphi}_0$ or $\delta\hat{\varphi}_{-2}$, and $\lesssim 10^{-3}$ for the other tests. The smaller errors for the former case are because frequency bands are constructed from a longer time to merger due to $\delta\hat{\varphi}_0 > 0$ or $\delta\hat{\varphi}_{-2} > 0$. In either case,

the errors are much smaller than unity, which shows our approximation is accurate enough for the analysis of GW190814.

V. CONCLUSION

In this paper, we have presented a rapid inference technique for parametrized tests of GR, one of the main tests of GR using gravitational waves from CBC. Our technique is based on a multiband decomposition of the gravitational-wave likelihood, which was originally developed for speeding up parameter estimation of CBC signals under the assumption of GR. It exploits the chirping nature of a signal and, in principle, is applicable to any chirp signal whose time to merger $\tau(f)$ is known. To extend this technique to parametrized tests of GR, we have derived $\tau(f)$ by taking into account non-GR deformations of the waveform. Applying the multiband decomposition technique with our new formula of $\tau(f)$ to a 1.4 $M_\odot$–1.4 $M_\odot$ BNS signal, we have found that our technique speeds up parametrized tests of a typical BNS signal by a factor of $\mathcal{O}(10)$ for the low-frequency cutoff of 20 Hz.

For validating our approximate technique, we have simulated BNS signals with SNRs of ∼50. Performing parametrized tests of them with and without our technique, we have verified that our technique produces results equivalent to those from runs without any approximate methods. We have also computed log-likelihood errors of our technique for GW190814 and confirmed that they are well below unity. Therefore, our work provides an efficient and accurate way of performing parametrized tests of GR, which is useful for dealing with more frequent detections in future observations.

We focus on single-parameter tests throughout this work. In principle, our technique can be applied to multiple-parameter tests using principal component analysis [18,25], with a modified time-to-merger formula parametrized by parameters corresponding to principal directions. We leave that extension as a future work.

ACKNOWLEDGMENTS

[1] B. P. Abbott *et al.* (LIGO Scientific and Virgo Collaborations), Phys. Rev. Lett. **116,** 061102 (2016).

[2] J. Aasi *et al.* (LIGO Scientific Collaboration), Classical Quantum Gravity **32,** 074001 (2015).

[3] A. Buikema *et al.* (aLIGO Collaboration), Phys. Rev. D **102,** 062003 (2020).

[4] M. Tse *et al.*, Phys. Rev. Lett. **123,** 231107 (2019).

[5] B. P. Abbott *et al.* (LIGO Scientific and Virgo Collaborations), Phys. Rev. Lett. **119,** 161101 (2017).

[6] F. Acernese *et al.* (Virgo Collaboration), Classical Quantum Gravity **32,** 024001 (2015).

[7] F. Acernese *et al.* (Virgo Collaboration), Phys. Rev. Lett. **123,** 231108 (2019).

[8] B. P. Abbott *et al.* (LIGO Scientific, Virgo, Fermi GBM, INTEGRAL, IceCube, AstroSat Cadmium Zinc Telluride Imager Team, IPN, Insight-Hxmt, ANTARES, Swift, AGILE Team, 1M2H Team, Dark Energy Camera GW-EM, DES, DLT40, GRAWITA, Fermi-LAT, ATCA, ASKAP, Las Cumbres Observatory Group, OzGrav, DWF (Deeper Wider Faster Program), AST3, CAASTRO, VINROUGE, MASTER, J-GEM, GROWTH, JAGWAR, CaltechNRAO, TTU-NRAO, NuSTAR, Pan-STARRS, MAXI Team, TZAC Consortium, KU, Nordic Optical Telescope, ePESSTO, GROND, Texas Tech University, SALT Group, TOROS, BOOTES, MWA, CALET, IKI-GW Follow-up, H.E.S.S., LOFAR, LWA, HAWC, Pierre Auger, ALMA, Euro VLBI Team, Pi of Sky, Chandra Team at McGill University, DFN, ATLAS Telescopes, High Time Resolution Universe Survey, RIMAS, RATIR, SKA South Africa/MeerKAT Collaborations), Astrophys. J. Lett. **848,** L12 (2017).

[9] B. P. Abbott *et al.* (LIGO Scientific, Virgo, Fermi-GBM, and INTEGRAL Collaborations), Astrophys. J. Lett. **848,** L13 (2017).

[10] R. Abbott *et al.* (LIGO Scientific, KAGRA, and Virgo Collaborations), Astrophys. J. Lett. **915,** L5 (2021).

[11] B. P. Abbott *et al.* (LIGO Scientific and Virgo Collaborations), Phys. Rev. Lett. **116,** 221101 (2016); **121,** 129902(E) (2018).

[12] B. P. Abbott *et al.* (LIGO Scientific and Virgo Collaborations), Phys. Rev. Lett. **123,** 011102 (2019).

[13] B. P. Abbott *et al.* (LIGO Scientific and Virgo Collaborations), Phys. Rev. D **100,** 104036 (2019).

[14] R. Abbott *et al.* (LIGO Scientific and Virgo Collaborations), Phys. Rev. D **103,** 122002 (2021).

[15] R. Abbott *et al.* (LIGO Scientific, Virgo, and KAGRA Collaborations), arXiv:2112.06861 [Phys. Rev. D. (to be published)].

[16] M. Isi, M. Giesler, W. M. Farr, M. A. Scheel, and S. A. Teukolsky, Phys. Rev. Lett. **123,** 111102 (2019).

[17] H. Takeda, S. Morisaki, and A. Nishizawa, Phys. Rev. D **103,** 064037 (2021).

[18] A. A. Shoom, P. K. Gupta, B. Krishnan, A. B. Nielsen, and C. D. Capano, arXiv:2105.02191.

[19] K. G. Arun, B. R. Iyer, M. S. S. Qusailah, and B. S. Sathyaprakash, Phys. Rev. D **74,** 024006 (2006).

[20] T. G. F. Li, W. Del Pozzo, S. Vitale, C. Van Den Broeck, M. Agathos, J. Veitch, K. Grover, T. Sidery, R. Sturani, and A. Vecchio, Phys. Rev. D **85,** 082003 (2012).

[21] C. K. Mishra, K. G. Arun, B. R. Iyer, and B. S. Sathyaprakash, Phys. Rev. D **82,** 064010 (2010).

[22] M. Agathos, W. Del Pozzo, T. G. F. Li, C. Van Den Broeck, J. Veitch, and S. Vitale, Phys. Rev. D **89,** 082001 (2014).

[23] L. Sampson, N. Cornish, and N. Yunes, Phys. Rev. D **87,** 102001 (2013).

[24] S. Perkins and N. Yunes, Phys. Rev. D **105,** 124047 (2022).

[25] M. Saleem, S. Datta, K. G. Arun, and B. S. Sathyaprakash, Phys. Rev. D **105,** 084062 (2022).

[26] N. Yunes, K. Yagi, and F. Pretorius, Phys. Rev. D **94,** 084002 (2016).

[27] P. Canizares, S. E. Field, J. Gair, V. Raymond, R. Smith, and M. Tiglio, Phys. Rev. Lett. **114,** 071104 (2015).

[28] R. Smith, S. E. Field, K. Blackburn, C.-J. Haster, M. Pürrer, V. Raymond, and P. Schmidt, Phys. Rev. D **94,** 044031 (2016).

[29] S. Morisaki and V. Raymond, Phys. Rev. D **102,** 104020 (2020).

[30] S. Vinciguerra, J. Veitch, and I. Mandel, Classical Quantum Gravity **34,** 115006 (2017).

[31] S. Morisaki, Phys. Rev. D **104,** 044062 (2021).

[32] B. Zackay, L. Dai, and T. Venumadhav, arXiv:1806.08792.

[33] N. J. Cornish, Phys. Rev. D **104,** 104054 (2021).

[34] F. Marion, in *Rencontres de Moriond Gravitational Waves and Experimental Gravity, Moriond Workshops*, edited by T. T. V. J. Dumarchez (The GIOI Publishers, Les Arcs, France, 2003), pp. 145–150.

[35] D. Buskulic (LIGO Scientific and Virgo Collaborations), Classical Quantum Gravity **27,** 194013 (2010).

[36] K. Cannon *et al.*, Astrophys. J. **748,** 136 (2012).

[37] C. M. Will, Proc. Natl. Acad. Sci. U.S.A. **108,** 5938 (2011).

[38] L. Blanchet, Living Rev. Relativity **17,** 2 (2014).

[39] A. Buonanno, B. Iyer, E. Ochsner, Y. Pan, and B. S. Sathyaprakash, Phys. Rev. D **80,** 084043 (2009).

[40] B. S. Sathyaprakash and S. V. Dhurandhar, Phys. Rev. D **44,** 3819 (1991).

[41] L. Blanchet and B. S. Sathyaprakash, Phys. Rev. Lett. **74,** 1067 (1995).

[42] D. M. Eardley, Astrophys. J. **196,** L59 (1975).

[43] P. Ajith *et al.*, Phys. Rev. D **77,** 104017 (2008); **79,** 129901(E) (2009).

[44] S. Husa, S. Khan, M. Hannam, M. Pürrer, F. Ohme, X. Jiménez Forteza, and A. Bohé, Phys. Rev. D **93,** 044006 (2016).

[45] S. Khan, S. Husa, M. Hannam, F. Ohme, M. Pürrer, X. Jiménez Forteza, and A. Bohé, Phys. Rev. D **93,** 044007 (2016).

[46] C. Van Den Broeck and A. S. Sengupta, Classical Quantum Gravity **24,** 155 (2007).

[47] C. Van Den Broeck and A. S. Sengupta, Classical Quantum Gravity **24,** 1089 (2007).

[48] R. O'Shaughnessy, B. Farr, E. Ochsner, H.-S. Cho, C. Kim, and C.-H. Lee, Phys. Rev. D **89,** 064048 (2014).

[49] E. Thrane and C. Talbot, Pub. Astron. Soc. Aust. **36,** e010 (2019); **37,** e036(E) (2020).

[50] N. Christensen and R. Meyer, Rev. Mod. Phys. **94,** 025001 (2022).

[51] N. Metropolis, A. Rosenbluth, M. Rosenbluth, A. Teller, and E. Teller, J. Chem. Phys. **21,** 1087 (1953).

[52] W. K. Hastings, Biometrika **57,** 97 (1970).

[53] J. Skilling, Bayesian Anal. **1,** 833 (2006).

[54] E. Poisson and C. M. Will, Phys. Rev. D **52,** 848 (1995).

[55] J. D. E. Creighton and W. G. Anderson, *Gravitational-Wave Physics and Astronomy: An Introduction to Theory, Experiment and Data Analysis* (Wiley-VCH, Weinheim, Germany, 2011).

[56] M. Maggiore, *Gravitational Waves. Vol. 1: Theory and Experiments*, Oxford Master Series in Physics (Oxford University Press, New York, 2007).

[57] LIGO Scientific Collaboration, LIGO Algorithm Library—LALSuite, free software (GPL) (2018).

[58] J. Veitch *et al.*, Phys. Rev. D **91**, 042003 (2015).

[59] G. Ashton *et al.*, Astrophys. J. Suppl. Ser. **241**, 27 (2019).

[60] I. M. Romero-Shaw *et al.*, Mon. Not. R. Astron. Soc. **499**, 3295 (2020).

[61] Data release for tests of general relativity with GWTC-2, https://dcc.ligo.org/LIGO-P2000438/public (2020).

[62] L. Santamaria *et al.*, Phys. Rev. D **82**, 064016 (2010).

[63] J. S. Speagle, Mon. Not. R. Astron. Soc. **493**, 3132 (2020).

[64] L. P. Singer and L. R. Price, Phys. Rev. D **93**, 024013 (2016).

[65] R. Abbott *et al.* (LIGO Scientific and Virgo Collaborations), Astrophys. J. Lett. **896**, L44 (2020).

[66] Gravitational Wave Open Science Center, GW190814, https://www.gw-openscience.org/eventapi/html/GWTC-2/GW190814/v2 (2020).

[67] S. Khan, K. Chatziioannou, M. Hannam, and F. Ohme, Phys. Rev. D **100**, 024059 (2019).

[68] S. Khan, F. Ohme, K. Chatziioannou, and M. Hannam, Phys. Rev. D **101**, 024056 (2020).

Correction: Figures 5 and 6 were erroneously interchanged during the proof process and have now been set right. Minor errors in the captions of Figs. 4 and 5 have been fixed.